


# Micro-Raman spectroscopy and complementary techniques applied for the study of copper and iron wastes from Motya (Italy)

Martina Bernabale<sup>1</sup> | Daria Montanari<sup>2</sup> | Lorenzo Nigro<sup>2</sup> |  
Federica Spagnoli<sup>2</sup> | Carmela Vaccaro<sup>3</sup> | Negar Eftekhari<sup>3</sup> | Maria Nicoli<sup>4</sup> |  
Caterina De Vito<sup>1</sup> 

<sup>1</sup>Department of Earth Sciences, Sapienza University of Rome, Rome, Italy

<sup>2</sup>Department Italian Institute of Oriental Studies—ISO, Sapienza University of Rome, Rome, Italy

<sup>3</sup>Department of Physics and Earth Science, University of Ferrara, Ferrara, Italy

<sup>4</sup>OGS Istituto Nazionale di Oceanografia e di Geofisica Sperimentale, Sgonico, Italy

## Correspondence

Caterina De Vito, Department of Earth Sciences, Sapienza University of Rome, P. le Aldo Moro 5, 00185. Rome, Italy.  
Email: [caterina.devito@uniroma1.it](mailto:caterina.devito@uniroma1.it)

## Funding information

Italian Ministry of Education, University and Research; PRIN 2017 Project People of the Middle Sea; Sapienza Università di Roma, Grant/Award Number: Ateneo funding, 2021

## Abstract

This work is the first archaeometric investigation on copper and iron wastes from the Phoenician site of Motya (Sicily, Italy), dating back to the 8<sup>th</sup> to the 4<sup>th</sup> century BC. The samples were analyzed through micro-Raman Spectroscopy ( $\mu$ -RS), Optical Microscopy (OM), Scanning Electron Microscope-Energy-Dispersive X-ray Spectroscopy (SEM-EDS), High-Resolution Field Emission Scanning Electron Microscopy (HR-FESEM), and Electron Micro-Probe Analysis (EMPA). Micro-Raman technique permitted to identify both primary phases, for example, calchopyrite, and secondary products such as cuprite and copper thrihydroxychlorides in the Cu-slugs and goethite in the Fe-slugs. SEM and HR-FESEM imaging showed the occurrence of inhomogeneous microstructures in the Cu- and Fe-slugs due to elements segregation, solidification, and corrosion. EMPA data revealed that the archaeometallurgical wastes from Motya can be differentiated on the basis of their chemical compositions. These preliminary results showed different typologies of by-products, such as base metals speiss, copper slugs from smelting sulfide ore with matte, and iron smelting and smithing slugs, suggesting different stages of copper and iron productions.

## KEYWORDS

Cu-slugs, EMPA, HR-FESEM, SEM-EDS, smithing slugs,  $\mu$ -RS

## 1 | INTRODUCTION

The slugs are very interesting materials for scientific studies because they give reliable information about processes that were undertaken from the ore to the final artifacts and, accordingly, about the nature of raw materials involved during the pyrometallurgical activities. The term slag includes different typologies of wastes obtained from pyrometallurgical processing of various ores.<sup>[1]</sup> In ancient

time, the extraction of base metals *via* pyrometallurgical process was a challenge due to the difficulty to separate ore minerals from its gangue to produce concentrate ore.<sup>[2]</sup> Over the time, the enhancement of mineral processing in the extraction of metals from ore-minerals influenced the quality of metallic materials and in turn led important technological development and drawbacks.<sup>[3,4]</sup>

Ancient metallurgical activities provided large amount of by-products as raw lumps and spills,

semifinished products, objects for repair or recycling, discharged ore, slag, matte and speiss as well as remains of tools and installations.<sup>[1,5–7]</sup> The great majority of ancient smelting slags is derived from processing of copper, iron, and lead ores.

Copper slags are composed by an assemblage made of oxides (iron, manganese, etc.), silicates as olivine, and pyroxene included in polymetallic matrices.<sup>[8]</sup> Their mineralogy is strictly related to the nature of the raw material involved in the processing and working conditions *via* pyrometallurgical process.<sup>[1]</sup> The main carriers of copper in the slags were Cu sulfides, oxides, and carbonate, for example, chalcopyrite ( $\text{CuFeS}_2$ ), digenite ( $\text{Cu}_9\text{S}_5$ ), chalcocite ( $\text{Cu}_2\text{S}$ ), bornite ( $\text{Cu}_5\text{FeS}_4$ ), cuprite ( $\text{Cu}_2\text{O}$ ), and malachite ( $\text{Cu}_2(\text{CO}_3)(\text{OH})_2$ ).<sup>[2,9,10]</sup>

Concerning the production of iron from its ores, two main steps are involved. First, iron oxide minerals must be reduced to produce metal in a solid state,<sup>[11]</sup> the so-called bloomery smelting or direct reduction method, using charcoal to heat the ore in a furnace. At temperatures above  $1000^\circ\text{C}$ , the combustion of gasses enriched in carbon monoxide reduced iron oxide to metallic state. Then, the bloom was refined to remove the adhered slags and shaped into objects during the smithing process.<sup>[11]</sup> All these activities can be carried out continuously at the same site. Alternatively, iron bar could have reached iron smithies through trade.<sup>[12]</sup>

However, it is not always easy to associate a waste to a given metallurgical process because the internal structure, chemical composition, and material performance of the object undergo changes continuously, especially during the long history of corrosion through time.<sup>[6,13,14]</sup> Therefore, in addition to common techniques as optical microscope, we decided to employ the capabilities of Raman spectroscopy, which can identify at the same time the mineralogical nature of the remaining original ore in the slag involved during the smelting process and discriminate between different polymorphs and corrosion products formed during the burial time. Raman spectroscopy represents an excellent tool in the investigation of Cultural Heritage field, not only because of its non-invasiveness but also because it allows the identification of the corrosion phases occurring at microscopic scale, providing a fingerprint of the compound under study.<sup>[15,16]</sup>

At the current state of knowledge, the technological skill of Phoenicians in metal production is still lacking for the Central Mediterranean area. Attempts to reconstruct the development of Phoenician metallurgy go back to the limited surveys of copper and iron production at Phoenician sites of the Iberian Peninsula, Sardinia, and North Africa.<sup>[17–21]</sup>

Among the most important Phoenician colonies, Motya had a strategic position in the Central Mediterranean area as it connected the sea routes of the East regions with those of the West of the Mediterranean. Moreover, Motya was located along the commercial routes of central Italy and received goods from the Center Europe to the North Africa.

Therefore, archaeometric studies on metal wastes from Motya are necessary to reconstruct the metallurgical background of Phoenician civilization in this area.

The archeological excavations at Motya carried out by “The Archeological Expedition at Motya of Sapienza University of Rome” (since the 2002) provided slags, dating back to the 8<sup>th</sup> to 4<sup>th</sup> century BC<sup>[22,23]</sup> along with weapons and other copper and iron artifacts.<sup>[24,25]</sup> This discovery implies that metallurgical activities of ore or semigrade of importation probably occurred in the first phase of Phoenician occupation of the island and in the central period of life of the city.

The diachronic study of material culture of Motya is a key-target because of the role of cultural mediator that the island held between the 8<sup>th</sup> and 6<sup>th</sup> century BC, before the rise of the power of Carthage.

Metallic material from Motya allows following the changes in technologies and manufactures, recognizing technological innovations and, indirectly, reconstructing the flows of ideas and goods.<sup>[26]</sup> Furthermore, Phoenicians were renown in ancient times for their skill in working metals, which they transformed into objects of great value. For this reason, it is likely that Phoenicians themselves were probably “metal producers” and/or at least “diffusers” of technological transfer and advancements of the *ars flaturae* during the first centuries of the first millennium BC.<sup>[27]</sup>

The aim of this work is to characterize a set of slags from Motya, dating back from the 9<sup>th</sup> to the beginning of the 8<sup>th</sup> century BC and to reconstruct the smelting process and nature of the raw material involved in different archeological frames and periods.

Data on mineralogy, microstructure, and chemical composition of waste products are necessary to obtain information about ore minerals, smelting temperatures, viscosity, different steps of metal reduction, efficiency of the process, redox conditions, cooling rates, and so on.<sup>[6,14,27,28]</sup>

Finally, the effects of corrosion on the original microstructure of the slags from lagoon-like environment are also evaluated as they continuously change during corrosion history.

A multi-analytical approach, based on SEM-EDS, HR-FESEM, EMPA and  $\mu$ -RS, has been involved to explore microstructure, chemical, and mineralogical composition of the slags.<sup>[29–31]</sup>

## 2 | MATERIALS AND METHODS

### 2.1 | Materials

The 14 slags here studied (Figure 1 and Table 1) were collected from three different areas of the island of Motya, within each of the larger subunits and selected for the study. Samples after the discovery are cleaned and stabilized with a controlled procedure and preserved in a protected atmosphere with regulated temperature (18–20°C), relative humidity (45%–50%), and light intensity, in the storeroom of archeological finds, without corrosion resumption.

The choice of samples taken for analyses was based on the macroscopic assessment that they are related to both iron and copper metallurgical processes.

Macroscopically, the size and shape of the slags are variable. Half of these materials have not specific shape and are covered with a greenish layer of copper corrosion products. The other half of the samples shows heterogeneous colors ranging from black to yellowish. Sample MD.18.171 is characterized by a plano-convex shape, while the others show an irregular shape.<sup>[9]</sup>

Their context and chronology are documented, as follows:

The *Area D*, located in the southwestern slope of the acropolis of ancient city, lies at the center of the island. The excavations revealed the oldest settlement at Motya dating back to the Middle Bronze Age (16<sup>th</sup> to 14<sup>th</sup> century BC)<sup>[32]</sup> and the early occupation by the Phoenician. In this area was uncovered and excavated a big disposal pit, called F.1112, that showed signs of burning. These excavations revealed an impressive amount of potteries, small finds shells, animal bones, pollens and metal slags. The chronology of the pit ranges from the first half of the 8<sup>th</sup> to the mid of the 6<sup>th</sup> century BC. Six stratigraphic units (US), attributable to four depositional phases, were identified in the pit.

The archeological filling of the pit is the result of a series of events close in time, which have the most recent chronological limit in the mid-6<sup>th</sup> century BC. On this date, a radical rearrangement of the area takes place that modifies the plan and the urban layout and, probably, also its function.<sup>[33,34]</sup> The most recent samples are MD.16.91 and MD.18.65 (US.1111), dating to the beginnings of the end of the 6<sup>th</sup> century BC. Other samples refer to the earlier period: MD.18.23 and MD.18.61 (US.1112) are dated, basing on the pottery repertoire, to the end of the 7<sup>th</sup> to the mid of the 6<sup>th</sup> century BCE and MD.18.110, MD.18.114 (US.1406), MD.18.168 MD.18.171 (US.1407), and MD.17.140 (US.7204) dated to the mid of the 7<sup>th</sup> century BCE; MD.18.220 (US.1492) is dated back to the end of 8<sup>th</sup> to the first half of the 7<sup>th</sup> century BC.

The *Area C* is located on the southern part of the island, where a sacred compound, called Sacred Area of the Kothon, was uncovered in last decades. The sacred area is occupied by two main temples devoted to the Phoenician divine couple Baal and Astarte.<sup>[35]</sup> The slag MC.16.166 was found inside a votive pit (*favissa* F.5118) holding the cult installations and offerings of the temple of Baal removed during the numerous renovations

**TABLE 1** Summary of phase composition and smelting activity of the main groups of archaeometallurgical finds analyzed in this study

Samples	Chronology	Type of waste
MM.16.23, MM.16.24, MC.16.166	6 <sup>th</sup> to 4 <sup>th</sup> century BC	Copper
MD.18.61, MD.18.65, MD.18.114, MD.18.110, MD.18.23, MD.18.168, MD.17.140	7 <sup>th</sup> to mid 6 <sup>th</sup> century BC	Copper
MD.16.91, MM.16.6, MD.18.171, MM.18.220	8 <sup>th</sup> to 4 <sup>th</sup> century BC	Iron

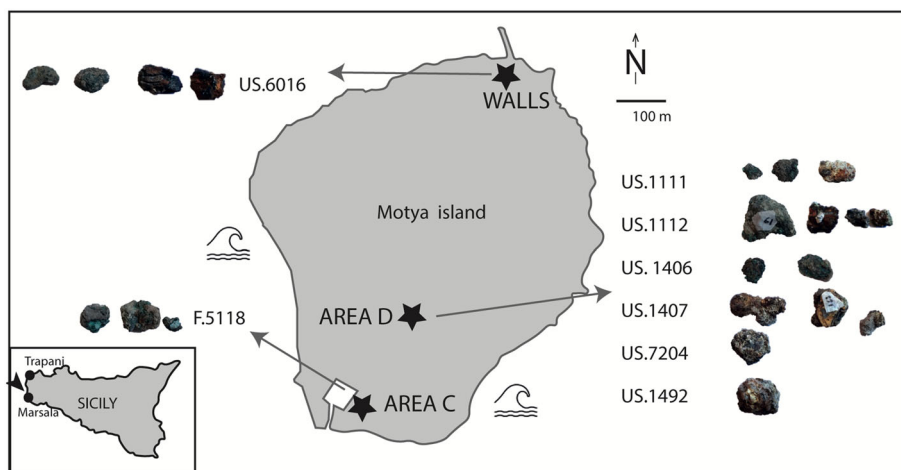


**FIGURE 1** A sketch map of the island of Motya indicating the location of the areas of the archeological excavation and the distribution of the samples [Colour figure can be viewed at [wileyonlinelibrary.com](http://wileyonlinelibrary.com)]

and restorations of the temple that occurred between the half of the 6<sup>th</sup> and the last quarter of the 5<sup>th</sup> century BCE.<sup>[23]</sup>

Finally, samples MM.16.6, MM.16.23, and MM.16.24 (US.6016) come from a late re-occupation after the destruction of Motya in 397/6 BC with industrial installation of this part of the City Walls (sector North) close to the North Gate.<sup>[36]</sup>

## 2.2 | Methods

The samples were first cut and then embedded in epoxy resin to produce cross-sections. These cross-sections were polished with SiC abrasive papers (grades from 800 to 4200) and finally with diamond paste (up to 1  $\mu\text{m}$ ) to produce perfect polished surfaces. OM, SEM-EDS, HR-FESEM,  $\mu$ -RS and EMPA were used.

Polished cross-sections prepared from the slag samples were examined under reflected light microscope using an Olympus BX60 at the Department of Earth Sciences, Sapienza University, Rome, Italy.

SEM-EDS investigations were carried out by FEI-Quanta 400 instrument, operating at 20 kV, equipped with X-ray energy-dispersive spectroscopy (Department of Earth Sciences, Sapienza University, Rome, Italy) and by ZEISS EVO40, 20 Kw, 90 Pa, at variable pressure and LaB<sub>6</sub> filament with a 20pA probe current (Department of Physics and Earth Science, University of Ferrara). SEM imaging was collected both in secondary electron (SE) and back scattered electron (BSE) modes. Energy-dispersive X-ray spectroscopy (EDS) spectra and X-ray maps were also used to show the distribution of the elements through the samples.

Representative samples were further investigated at nanometer scale using a Zeiss Auriga 405 microscope (HR-FESEM) at Sapienza Nanoscience and Nanotechnology Laboratories (SNN-Lab) of the Research Center on Nanotechnology Applied to Engineering (CNIS) of Sapienza University. The analyses were performed under an accelerating voltage of 20 kV, at a working distance of 10 mm.

In addition,  $\mu$ -RS was used on polished cross-sections to determine the mineralogical composition of slag phases. Micro-Raman measurements were performed by Jobin-Yvon Horiba LabRam spectrometer coupled with an Olympus BXFM optical microscope with objectives up to 100 $\times$ . The He-Ne laser line at 632.82 nm was used as excitation source. Laser power (17 mW at the source) was modulated using 25% natural density filter in order to keep it at a low level on the sample and thus to avoid laser-induced transformations. Raman spectra were recorded in the range of 100–1400  $\text{cm}^{-1}$  with an exposure

time of 5–15 s and two to four accumulations. The wavelength scale was calibrated using a Silicon standard (520.5  $\text{cm}^{-1}$ ), and the acquired spectra were compared with scientific published data and reference databases, such as Horiba LabSpec 6 (Horiba).

Quantitative chemical analyses were acquired using a Cameca SX50 electron microprobe equipped with five wavelength-dispersive spectrometers (CNR-IGAG, Rome, c/o Department of Earth Sciences, Sapienza University of Rome). The operating conditions were as follows: accelerating voltage 15 kV, beam current 15 nA, and beam size 15  $\mu\text{m}$ . Gallium arsenide was used as a reference standard for As (TAP, thallium [acid] phthalate crystal), periclase for Mg (TAP) apatite for P (TAP), wolastonite for Si (TAP) and Ca (PET, penta-erythriol crystal), magnetite for Fe (LIF, lithium fluoride crystal), rhodonite for Mn (LIF), rutile for Ti (PET), barite for S (PET), potassium chloride for Cl (PET), orthoclase for K (PET) copper for Cu (LIF), galena for Pb (PET), tin for Sn (PET), and gold alloy (20%) for Ag. By EPMA, it was possible to accurately determine the chemical compositions of the phases present in the slags with an analytical error  $\sim$ 1% rel. For the major elements and detection limit between 0.01 and 0.1 wt.%.

## 3 | RESULTS AND DISCUSSION

### 3.1 | Microstructure and qualitative chemical analysis of the slags

SEM-EDS analysis and HR-FESEM imaging highlight differences in microstructure and composition among the different slags and suggest the preliminary grouping into different types, *i.e.*, copper-working wastes (A, B, C) and iron slags (D,E), respectively.

#### 3.1.1 | Type a

Samples MM.16.23, MM.16.24, and MC.16.166 (Type A) show a core composed by a Cu-rich matrix and Cl-phases, interrupted by numerous blackholes (Figure 2A). BSE image (Figure 2B) highlights that chlorine occurs in the intergranular positions, acting as corrosive agent of the copper matrix. Large inclusions of copper sulfide occur in the bulk, still preserved in the corrosion layers. Stratified layers of copper-chlorine oxides occur in the patina and suggest progressively more oxidizing conditions towards the external surface of the sample. The external patina includes also soil components made of Al, Si, Ca, Fe, and quartz crystals.



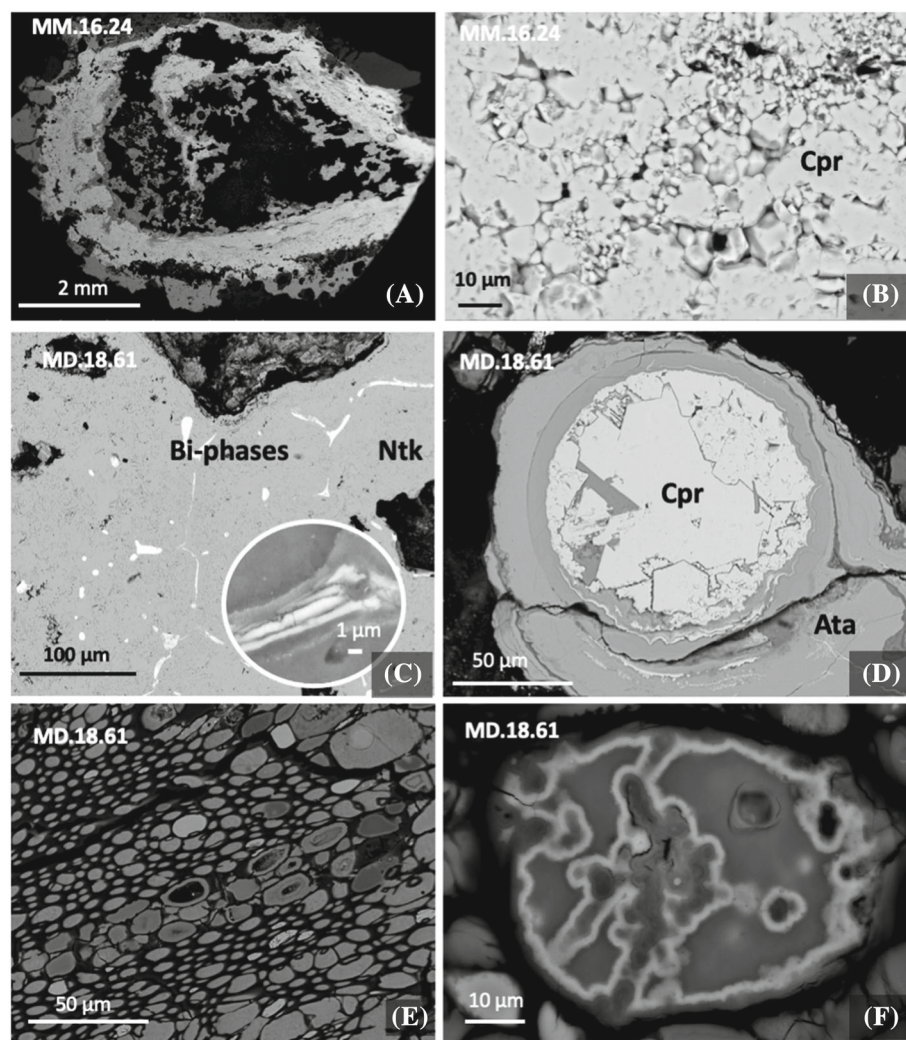


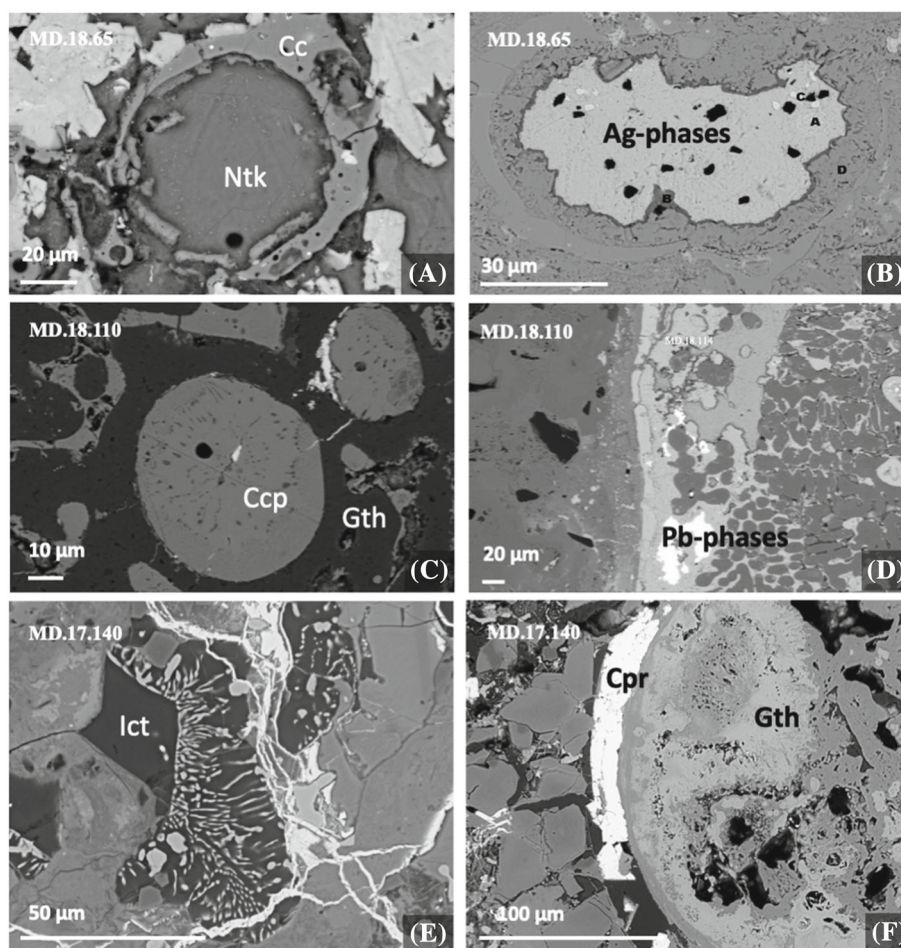
**FIGURE 2** (A) Scanning electron microscope-back scattered electron (SEM-BSE) image of microstructure in sample MM.16.24. (B) Intergranular corrosion by chlorine in the cuprite matrix. (C) SEM-BSE image and FESEM magnified view showing Bi inclusions that occur as thin filaments in the pale gray phase. (D) Cubic crystals of postdepositional cuprite filling pores and cracks. (E) Wood cell texture consisting mainly of Cu-Ca-Si-O-P-Mg. (F) Field emission scanning electron microscopy (FESEM) image showing Cu-Si-O crystal with impurities of Ni, Zn, Co, P, Cl, in the light edges. Labels in the photos: cpr = cuprite, ntk = nantokite, ata = atacamite

### 3.1.2 | Type B

Compared with Type A, these samples (MD.18.61, MD.18.65, MD.18.114) contain other metals and metalloids as Sb, As, and Bi. Sample MD.18.61 contains Bi-rich inclusions (approximately 61 wt.% of Bi, 17 wt.% of Cu, 9 wt.% of O, 13 wt.% of Cl) as showed by SEM-BSE imaging. The inclusions occur as thin filaments between Cu-grains as highlighted by HR-FESEM image at high magnification (Figure 2C). The altered bismuth inclusions could be impurities of the raw ore, for example, chalcopyrite. Spheroidal crystals of postdepositional cuprite fill pores and cracks, which are related to bubbles gas in the slag (Figure 2D). Close to the surface of this sample, a wood cell texture with granulated blebs of Cu-Ca-Si-O-P-Mg appears oriented and elongated according to preferential directions (Figure 2E). This texture is attributed to charcoal remains<sup>[37]</sup> as the pores are filled by Cu silicate enriched in CaO. During burning, charcoal produces a fuel ash, typically enriched in lime (CaO), alkali, MgO, and P<sub>2</sub>O<sub>5</sub>, which acts as a flux lowering the temperature

of melting and involving the formation of slag enriched in such elements. Figure 2F shows a Cu-Si-O crystal with impurities of Ni (approximately 10 wt.%), Zn (approximately 5 wt%), and Co (approximately 5 wt%), which can be incorporated into the structures of silicates, replacing Fe and/or Mg due to their similar ion radii. Phosphorous (approximately 2 wt%) and Cl (approximately 1 wt.%) also are present as soil contaminants. The presence of cobalt is not common in fuel ash; therefore, the occurrence of this element can be explained with the use of Cu-raw material with Co-bearing sulfur minerals.<sup>[37]</sup> Figure 3A shows a dendritic structure of Sb-rich compounds (white phase) and Cu-rich area (gray phase) of the sample MD.18.65. Small inclusions of Cu-sulfides with chalcocite-like composition (pale gray phase) are enclosed in Cu-Cl microdomains of rim (Figure 3A). This cupriferous antimonide can be attributed to speiss production.<sup>[14]</sup> As speiss and matte are partially miscible, they could form separate melts in the furnace.<sup>[38]</sup> The co-presence of antimony (approximately 53 wt.%) and arsenic (approximately 9 wt.%) suggests the use of fahlre as

**FIGURE 3** (A) Field emission scanning electron microscopy (FESEM) image showing the segregation of microdomains of Sb-rich compounds (white phase) separate from Cu-Cl droplet (gray phase). (B) Scanning electron microscope-backscattered electron (SEM-BSE) image of Ag-inclusion strongly corroded by chlorine. (C) FESEM image showing individual round inclusions of copper-iron sulfides in the center area of the section MD.18.110. (D) FESEM image showing the interface between slag and prills, showing dark spheroidal grains of a goethite in a copper matrix mottled with iron precipitated from solid solution. Small irregular Pb inclusions are embedded in the slags. (E) BSE image of sample MD.17.140 showing cuprite veins associated with melted silicates and iron oxides and melted potassium feldspar. (F) Cuprite vein surrounded a big globule of Fe oxide. Labels in the photos: cc = chalcocite, ntk = nantokite, ccp = chalcopyrite, gth = goethite, lct = leucite, cpr = cuprite



raw material. It is known that volatile elements as antimony and arsenic are partially lost during roasting, whereas direct reduction smelting will retain a large proportion of these elements.<sup>[39,40]</sup> These results suggest that raw materials do not suffer a “dead-roasting” process. Figure 3B shows the occurrence of Ag-rich inclusions in gray matrix made of copper oxide, probably deriving from Ag-rich copper ores. These inclusions are strongly corroded by chlorine present in lagoon-like environment of Motya. In addition, Sb-rich inclusions also occur in the corroded copper matrix of sample MD.18.114.

### 3.1.3 | Type C

Slags MD.18.110, MD.17.140, and MD.18.23 (Type C) consist of two phases, formed by the segregations of copper-rich and an iron-rich phase (Figure 3C). In particular, the microstructure is dominated by mixed copper-iron sulfides embedded in the interdendritic gray phase composed by  $\text{FeO}_x$  with some impurities of copper. According to Ellingham diagrams,<sup>[41]</sup> in a system containing copper, iron, oxygen, and sulfur, Fe forms iron oxide, which is absorbed into the slag melt, whereas Cu

preferentially bonds sulfur to form matte as a separate melt phase.<sup>[42]</sup> Finally, small rounded-phases, containing Pb, Fe, O, are included in the slags (Figure 3D). Lead occurs in combination with smelted raw copper or as secondary inclusions precipitate in pores and voids. Slag MD.17.140 (Figures 3E,F) contains numerous veins of copper oxide in association with iron oxides and melted potassium and aluminum silicates. BSE imaging and X-ray maps of slag MD.18.168 (Figure 4A) show the microstructure and the distribution patterns of Cu, Fe, O, Cl, S, Si, and Ca. Particles of quartz occur in the matrix and in the external surface of the slag. Crystals of quartz probably derive from unmelted gangue (or flux) occurring in the furnace charge. In fact, the presence of quartz in the slag is due to low temperature in the furnace and insufficient melting time, that is, kinetic effect or overestimation of the  $\text{SiO}_2$  flux in the charge.<sup>[43,44]</sup>

In addition, the detection of chlorine also in these samples is the result of soil contamination, as the settlement of Motya is situated in the Mediterranean coast. The Cl-content increases in Cu-rich matrix from the top to the bottom of the section, suggesting a different exposure of the sample to chlorine attack (Figure 4B). In fact, Cu is progressively converted into copper chloride-



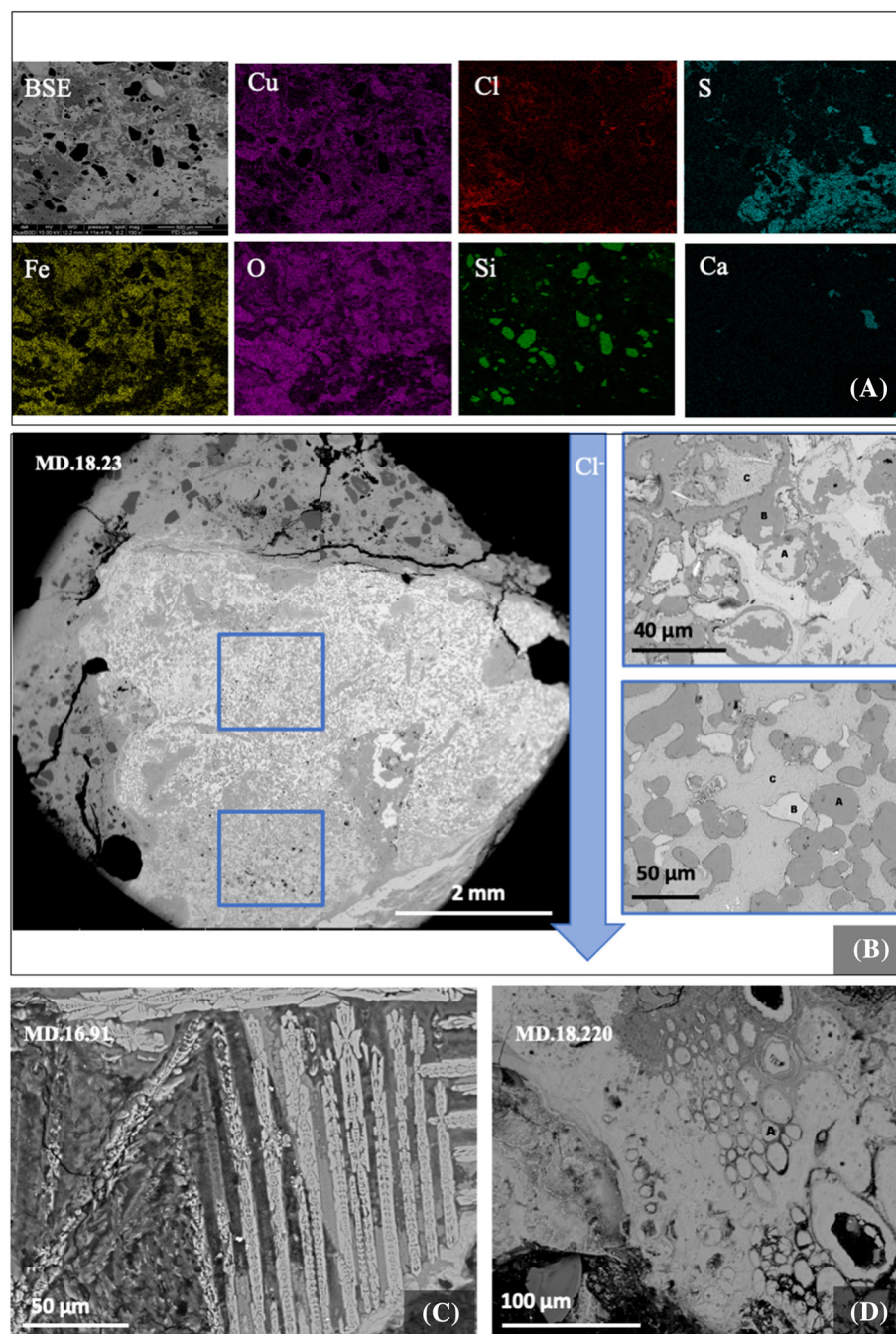


**FIGURE 4** (A) Back scattered electron (BSE) imaging and X-ray maps, showing the microstructure and the compositional variation of the Cu, Cl, S, Fe, O, Si, and Ca in sample MD.18.168. (B) BSE imaging showing the microstructure and the compositional variation of Cl, Fe, Cu, O, and S, in sample MD.18.23. From the top to the bottom of the sample is observed an increasing of chlorine in the Cu-rich matrix. (C) BSE image of well-crystallized chain of fayalite. (D) Hematite oolites in sample MD.18.220. Labels in the photos: Fa = fayalite [Colour figure can be viewed at [wileyonlinelibrary.com](http://wileyonlinelibrary.com)]

microdomains towards the bottom of the sample. The presence of Cu sulfide throughout sample indicates the desulfurization processes; that is, the conversion of Cu-S into metal is not completed.

### 3.1.4 | Types D-E

Among slags, samples MD. 16.91, MM. 18.220, MM.18.171, and MM.16.6 differ widely from the others as they present an Fe-composition. These samples are characterized by the typical reddish-brown color of

the rust, numerous degassing pores, and by the absence of copper inside. Despite smelting and smithing slags are very difficult to distinguish, two types of slags are recognized: Iron smelting slags (Type D) are essentially composed of fayalite, whereas hammerscales (Type E) produced during the later stages of smithing and forging are smaller and more enriched in iron oxides.

Sample MD. 16.91 (Type D) of Figure 4C is characterized by parallel elongate chains of fayalite that suggest a low melting point at 1481 K (1208°C).<sup>[45]</sup> Indeed, iron oxide starts to react with silica to form molten olivine-bearing ferrosilicate slags in the range thermal rang of

1000–1100°C. Moreover, fayalite morphology is a function of cooling rate. Chain olivines in Figure 4C indicate an intermediate cooling rate in the range 50–200°C/h.<sup>[46]</sup> On the other hand, the large occurrence of iron oxides suggests that the amount of iron oxide in the molten system exceeds that required to bind all silica, leading to the crystallization of different Fe oxides depending on redox conditions of the system.<sup>[47]</sup>

Samples MM. 18. 220, MM.18.171 and MM.16.6 (Type E) are characterized by porous structures and mainly composed by iron oxides. Figure 4D shows the presence of iron oolites that formed by weathering and precipitation of iron-bearing solutions in the charcoal pores.

An interesting feature of sample MD.18.171 is the presence of spheroidal aggregates that contain Ca and Mg.

### 3.2 | Mineralogical characterization of slags and corrosion products

Micro-Raman spectra<sup>[48,49]</sup> of the Cu-slugs (*i.e.*, Types A and B) indicate that the main phases are cuprite and copper thrihydroxychlorides along with small quantities of sulfide minerals such as covellite (Figure 5) inside the oxidized matrix.

Cuprite (Cu<sub>2</sub>O), with the typical vibrational bands at 146, 216, 629 cm<sup>-1</sup>, appears in Types A, B, and C as secondary corrosion product in the corroded area of the sample (Figure 5A,E) or as primary phase of the smelting process, which is related to fairly reducing conditions in the furnace.

Among hydroxychlorides, both clinoatacamite and atacamite (Cu<sub>2</sub>Cl(OH)<sub>3</sub>) are present in copper waste of Types A and B as corrosion compounds, resulting by bronze disease (Figure 5A,E). According to earlier studies<sup>[50–52]</sup> different species of hydrated copper chloride were recognized. Raman bands at 824, 910, 978 cm<sup>-1</sup> suggest the presence of atacamite (Figure 5E), whereas those at 800, 895, 926 cm<sup>-1</sup> are attributed to clinoatacamite (Figure 5A).

In sample MD.18.61 (Type B), the main vibrational bands at 184, 210, 311, and 448 cm<sup>-1</sup> are attributed to bismuth oxide, that occur as thin elongated inclusions (Figure 5D).

The main vibrational bands of covellite (Cu-S) are identified at 257 and 461 cm<sup>-1</sup> (Figure 5B) in all types of copper slags. Covellite is a typical alteration product of weathering of sulfides due to water circulation, which penetrates through fractures and pores. The alteration process proceeds from the outside of the grains towards the inside. Frequently, covellite is intimately associated

with iron hydroxides, for example, goethite, formed by iron leached from sulfides.<sup>[53]</sup>

The presence of minor amounts of malachite (Cu<sub>2</sub>(OH)<sub>2</sub>CO<sub>3</sub>) in sample MC.16.166 (Type B) is identified by the main bands at 147, 420, 1086, and 1493 cm<sup>-1</sup> of Raman spectrum (Figure 5C).

Raman data of copper slags from smelting sulfide ore with matte (Type C) reveal that the numerous small pits, that characterize the microstructure, contain particles of chalcopyrite as indicated by the main bands at ≈272 and 326 cm<sup>-1</sup> (Figure 5F). Chalcopyrite (CuFeS<sub>2</sub>) occurs as dispersed globules, being the last phase that solidifies in the system with a melting point of about 950°C.<sup>[54]</sup> The analysis performed on the dark gray matrix shows the typical peak of goethite at 298, 385, 550 cm<sup>-1</sup> (Figure 5F). Also in this case, the occurrence of goethite is the result of weathering process in burial condition.

The presence of leucite (KAlSi<sub>3</sub>O<sub>6</sub>) in sample MD.17.140 (Type C) is confirmed by the two main bands at 487 and 519 cm<sup>-1</sup> (Figure 5G); it occurs as euhedral crystals in association with magnetite. The residual melt is enriched in Fe with a typical eutectoid microstructure, which is composed of fine grain-sized of magnetite and leucite.<sup>[53]</sup> Generally, high contents of iron and the low silica and/or lime in the molten slag involve the formation of crystals of olivine rather than pyroxene<sup>[55]</sup> and the precipitation of magnetite (Figure 5H) and SiO<sub>2</sub> undersaturated feldspathoids as leucite. The presence of leucite also suggests an initially high content of K in melt slag.<sup>[44]</sup>

Raman spectrum of sample MD.17.140 confirms the presence of goethite in the pale gray globules and of calcite in the gray matrix (Figure 5H).

The mineralogy of the iron slags is composed by a heterogeneous mixture of silicates, for example, fayalite in Type D and iron oxides, that is, hematite (α-Fe<sub>2</sub>O<sub>3</sub>), wustite (FeO) in Type E, as well as alteration products such as goethite, lepidocrocite, and hematite (α-Fe<sub>2</sub>O<sub>3</sub>).

Wustite was identified according to the main band at approximately 652 cm<sup>-1</sup>.

Over time, Fe-oxide products change from lepidocrocite (orange phase) to goethite (dark area) or hematite at high temperatures (Figure 5I,J). Goethite is an isolating phase, whereas lepidocrocite, a stable polymorph of goethite, represents the active phase in the corrosion process.<sup>[56]</sup> Goethite is the most stable iron oxy-hydroxide, identified by bands at 242, 298, 388, 480, and 552 cm<sup>-1</sup> in all iron slags. The Raman bands of lepidocrocite are well identified at 215, 248, 309, 373, and 520 cm<sup>-1</sup> in Type E. Raman spectrum of sample MD.16.91 (Type D) (Figure 5K) shows the following shifts at 229, 279, 812, 833, and 895 cm<sup>-1</sup> which are attributed to fayalite that crystallize at 1100–1200°C.



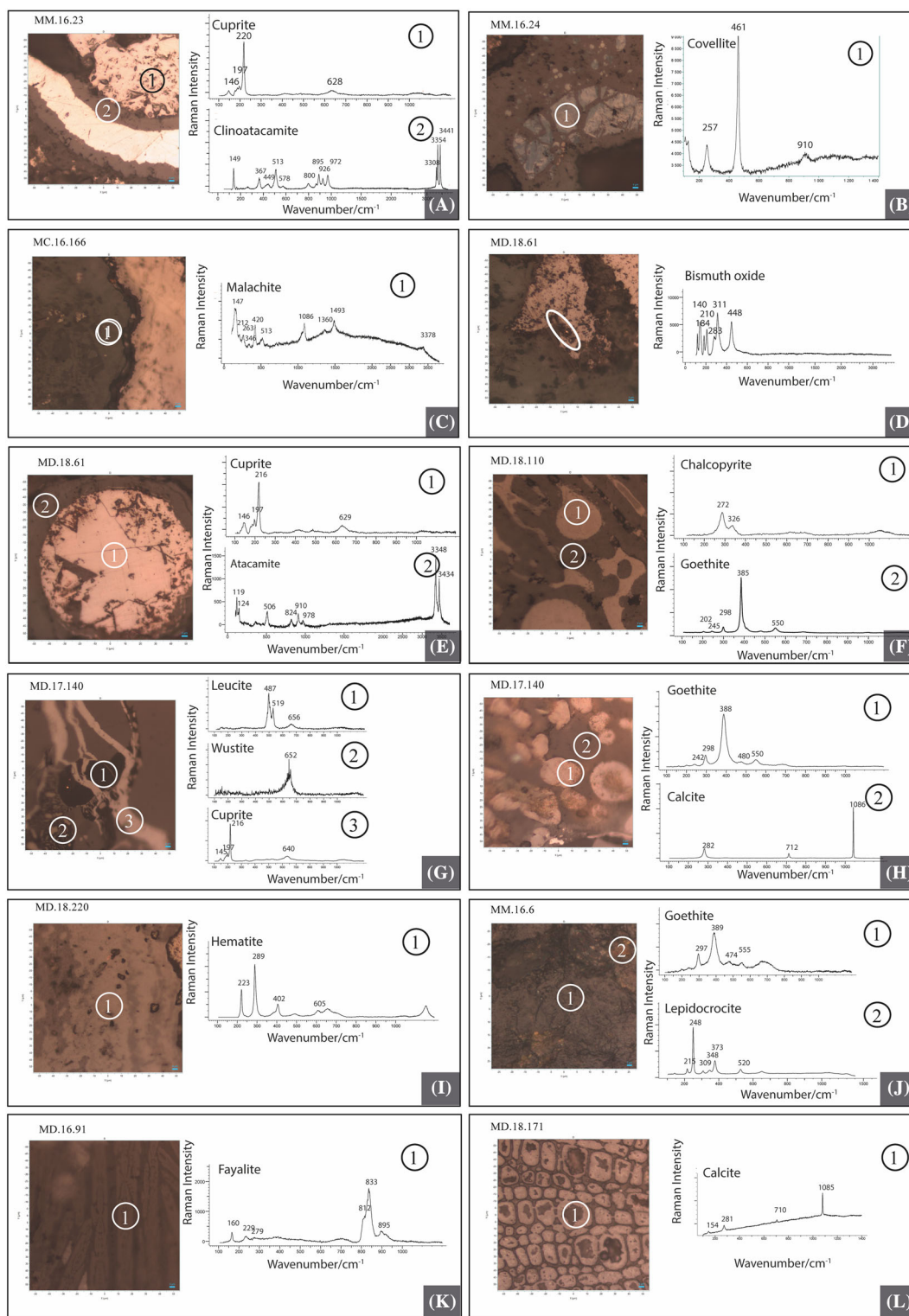


**FIGURE 5** Raman spectra of minerals: (A) (1) cuprite, (2) clinoatacamite. (B) Covellite. (C) Malachite. (D) Bismuth oxide. (E) (1) cuprite, (2) atacamite. (F) (1) chalcopyrite, (2) goethite. (G) (1) leucite, (2) wustite, (3) copper oxide. (H) (1) goethite, (2) calcite. (I) Hematite. (J) (1) goethite, (2) lepidocrocite. (K) Fayalite. (L) Calcite [Colour figure can be viewed at [wileyonlinelibrary.com](https://onlinelibrary.wiley.com/terms-and-conditions)]

In Type E calcite fills, the cavities of the cells and the intercellular matrix of the granulated aggregate (Figure 5L).

The preliminary results are reported in Table 2 with a qualitative estimation of the abundance of the different mineral phases. The abundance of each mineralogical

TABLE 2 Qualitative abundance of mineralogical phases: x = present, xx = abundant, xxx = very abundant

Sample	MM.16.23	MM.16.24	MC.16.166	MD.18.61	MD.18.65	MD.18.114	MD.18.110	MD.18.23	MD.18.168	MD.17.140	MM.16.6	MD.16.91	MD.18.171	MD.18.220
<b>Silicates</b>														
Leucite									x					
Fayalite											xxx			
Quartz	x	x		x			x	xx	x	x	xx	x		
Pyroxene							x							
<b>Oxides</b>														
Magnetite												x	x	
Wustite									x					
Hematite											x	x	x	x
Lepidocrocite											x			
Cuprite	xxx	xxx	x	xx		xxx	x		xx	xx				
Goethite							xx	xxx	xxx	xxx	xxx	xx	xxx	xxx
<b>Chlorides</b>														
Clinoatacamite	xx			x		xx								
Atacamite		xx	x	x					x					
Nantokite	x	x	xx	xxx	xxx	xxx	xx	xx						
<b>Carbonates</b>														
Malachite			x											
Dolomite				x									x	x
Calcite													x	
<b>Sulfides</b>														
Chalcocite/ covellite	xx	x			x		xx	xx	xx	x				
Chalcopyrite						xx								
<b>Sulfates</b>														
Gypsum				x					x					
<b>Metals/ Metalloids</b>														
Cu	x		xxx	x			xx	xx	x	x				
Bi				x										
Sb					xxx	x								
As					x									
Pb				x			x							
Ag					x									

phases was assessed combining the use of reflected light microscopic analysis, SEM-EDS, as well as micro-Raman spectroscopy.

### 3.3 | Quantitative chemical analysis and phase diagrams

Major and minor elements of the bulk of Motyan slags are measured by EMPA with the aim to classify them through quantitative chemical data.<sup>[44,57]</sup>

The results indicate that the Cu-based slags are mainly composed of Cu (0.35–99.69 wt%) and Fe (0.00–50.05 wt%) that suggest a considerably variability of the chemistry (Table S1). The slags MD.18.110, MD.18.168, MD.18.23, and MD.17.140 are richer in Fe, S, Ca, and Si and depleted in Cu, Cl, As, and Sb compared with the other samples (Table S1). Minor constituents are P (0.00–8.36 wt%), Al (0.00–5.23 wt%), K (0.00–1.08 wt%), Ag (0.00–90.08 wt%), Pb (0.00–49.28 wt%), Ni (0.00–0.78 wt%), Co (0.00–0.89 wt%), and Zn (0.00–1.89 wt%). The total elemental composition for some analytical points is not 100 wt%. The remaining contents for the rest of the total mass would be oxygen and/or water.

Instead, the chemical compositions of the three Fe-rich samples (*i.e.*, MM. 16.6, MD. 16.91, MD.18. 171) are reported in Table S2. These slags are mainly formed by iron oxides, SiO<sub>2</sub>, and CaO. Minor amounts of MnO, Al<sub>2</sub>O<sub>3</sub>, and MgO also occur. The content of SiO<sub>2</sub> and iron oxides shows wider variation (overall ranges of 0.02–43.94 wt.% and 0.43–87.89 wt.%), whereas the CaO content varies from 0.06 to 53.43 wt.%.

The results of Fe-rich slags have been plotted within CaO-FeO-SiO<sub>2</sub> ternary system<sup>[58]</sup> (Figure 6). This ternary diagram gives the composition of the main phases in the slags, due to different contributions of clays, fuel ash, and ore.<sup>[59]</sup> In fact, during the smelting and smithing of iron, a small amount of ash was produced by the combustion of charcoal fuel, contributing to the composition of the slag. The chemical composition of the slag is driven by the furnace temperature, redox conditions, reaction speed, and chemical composition of the materials present in the smelt.<sup>[60]</sup> In particular, olivine and wuestite provide precious information about the iron smelting-smithing process. Olivine is the most abundant silicate with variable between fayalite (Fa, Fe<sub>2</sub>SiO<sub>4</sub>) and kirschsteinite (Kst, CaFeSiO<sub>4</sub>).<sup>[61]</sup> Plotting the data on the equilibrium ternary diagram (Figure 6), only sample MD.16.91 is grouped into the fayalite field, corresponding to the lowest liquidus temperatures in this slag system (1100–1250°C). We can conclude that this slag is formed under well-controlled reducing conditions. On the contrary, most samples fall in the area of iron oxides,

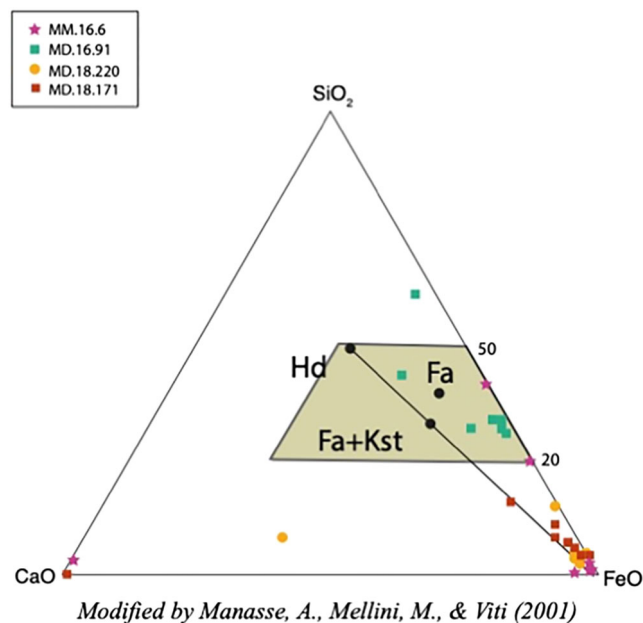


FIGURE 6 CaO-FeO-SiO<sub>2</sub> ternary system. Sample MD.16.91 fall into the fayalite region, while samples MM.16.6, MD.18.220, MD.18.171 fall in the area of FeO [Colour figure can be viewed at [wileyonlinelibrary.com](http://wileyonlinelibrary.com)]

indicating that iron oxide in the molten system exceeds the amount required to combine all the silica; therefore, the excess of iron in the system favored the crystallization of various iron oxides.<sup>[62]</sup>

### 3.4 | Classification of slags

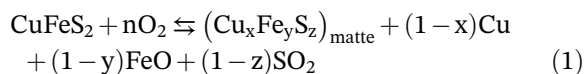
Data on microstructure, mineralogy, and chemistry of the slags suggested that the samples can be classified in copper and iron slags.<sup>[13,63]</sup>

Type A corresponds to the more recent Motyan copper production, dating back to the 6<sup>th</sup> to the 4<sup>th</sup> century BC. The data show high amount of copper with numerous Cu-S inclusions. No significant amounts of alloying elements such as Pb, Sb, or As are detected in the composition of this group of materials. The presence of chlorine is responsible of the secondary corrosion microstructures and leads to dangerous cyclic of copper corrosion.<sup>[52]</sup> Indeed, when cuprous chloride, located in the internal layers of the samples, is exposed to the atmospheric humidity, it reacts with oxygen and water cycles to form green copper oxychloride, that is, atacamite and its polymorphs, that react with copper to form new cuprous chloride and water. In this way, the reaction restarts and new atacamite and cuprite are formed. The possible reasons for the occurrence of these waste could be explained as products of a final refining stage of a copper metallurgy.<sup>[64,65]</sup>

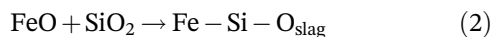


Type B, dating to the mid of 7<sup>th</sup> to mid of the 6<sup>th</sup> century BC, is mainly composed by copper with minor amounts of Sb, As, and Bi. These wastes are considered the remains of base-metal speiss, that is, a complex mixture of copper arsenides and antimonides, often containing sulfur and lead. Because they are brittle and cannot be processed otherwise than by casting, they are considered waste.<sup>[14]</sup> Although part of arsenic and antimony is converted from “primary ore process” into gasses (i.e., during roasting and smelting) high contents of these elements remain in the speiss. The loss of these elements may be caused primarily by the conditions of the smelting and melting (the evaporation rate of arsenic is higher under oxidizing conditions), the length and intensity of the working techniques when shaping the objects, and the possibility of recycling.<sup>[66]</sup> In sample MD.18.65, silver occurs in association with silver chlorides. Silver could get trapped in the speiss instead of in Pb, whence it may be separated via cupellation. The typical fahlore composition, with arsenic and antimony in the per cent and silver and bismuth in the per mille ranges, appears only in the Early Bronze Age.<sup>[67]</sup>

Type C, dating to the mid of the 7<sup>th</sup> to the mid the 6<sup>th</sup> century BC, suggests the presence of metallurgical activity in Moya, producing copper from sulfide raw materials (probably chalcopyrite) by partial smelting of ores, which leads to the formation of slags with large quantities of impurities such as sulfur and iron, following the reaction:



During smelting process, iron is partially enriched in the siliceous gangue of ore and produces a slag following reaction 2<sup>[68]</sup>:



The presence of iron–copper sulfide and poorly slagged iron oxides of this sample suggests that the transformation of copper–iron sulfidic minerals (e.g., chalcopyrite, bornite, covellite, and chalcocite) into metal is stopped before the complete reaction, probably due to the low temperature of processing.<sup>[68]</sup> Thus, part of Fe is retained in the Cu-sponge as iron oxide, and the remaining Fe concurs to form matte.<sup>[69]</sup>

Mineralogical data and chemical composition of major and minor elements revealed that the most ore minerals used for copper production are fahlore and chalcopyrite. This assemblage was typical of the Montevecchio–Ingurtosu district (SW Sardinia) and Peloritani mineralization.<sup>[70,71]</sup>

Types D and E, dating to the 8<sup>th</sup> to the 4<sup>th</sup> century BC, are Fe-rich slags. On the base of macroscopic features (i.e., shape, dimensions) and chemical and mineralogical markers, two types of slags are distinguished: Type D is a furnace slag, containing many inclusions of fayalite corresponding to the primary process of iron production, while the slags of Type E are hammerscales corresponding to materials removed during smithing, when the bloom was heat-treated in the hearth and hammered on the anvil to produce the iron artifact. In this case, iron exists in the form of oxides or oxyhydroxides. Charcoal is often included in this material. In some cases, a significant amount of Ca occurs, probably used as flux in later stages of the processing of iron ore.

The results suggest the co-existence of different procedures at Motya. Local metallurgical remains reveal differences between the more ancient methods (the 8<sup>th</sup> to the 6<sup>th</sup> century BC) and the innovations introduced by Eastern Mediterranean settlers and traders in the 6<sup>th</sup> to the 4<sup>th</sup> century BC.<sup>[72]</sup>

Concerning Fe-production, the slags dating to the 8<sup>th</sup> to the 4<sup>th</sup> century BC indicate a technological development from old to more recente samples. In particular, the results suggest that smelting process of iron and copper is concentrated in the 7<sup>th</sup> to the 6<sup>th</sup> century BC (the *area D* of the island). However, the co-occurrence of smelting and smithing iron slags suggests that some contamination occurred. In addition, evidence of speiss as an intermediary product for the manufacture of copper-alloys has been reported in the Near East.<sup>[14,42,73]</sup> On the other hand, samples MM.16.6, MM.16.23, and MM.16.24 excavated from the industrial area of the City Walls—that was built after the destruction of Motya in 397/6 BC—belong to the more recent metallurgical activities of refining of copper and iron to produce artifacts.

## 4 | CONCLUSION

Microstructure, mineralogy, and chemistry of Cu- and Fe-slugs from the archeological site of Motya indicated the occurrence of different types of archeometallurgical remains, that is, base metals speiss, copper slags from smelting sulfide ore with matte, and iron smelting and smithing slags. In particular,  $\mu$ -RS, SEM, HR-FESEM, and EMPA results shed new light on the operating parameters of the smelting process, such as the temperature, redox conditions, and the efficiency of separation between slag and metal.

In addition, the preliminary study allowed a comparison between parts of the site that might correspond to different areas and periods. In conclusion, different stages

of working processes were recognized: Evidence of copper and iron smelting process demonstrated an attempt to extract both the metals; the presence of hammerscale in Motya confirms that iron smithing took place in Motya.

Moreover, the present results identify evidence of matte and speiss, suggesting a polymetallic character of the smelted ore. The occurrence of copper-iron sulfides (corresponding to unreduced ore) suggested that there had been insufficient time or temperature for matte to dissolve before the metal was tapped. Future investigations on higher population sampling will provide a clearer view of possible relationship between the development of copper and iron working in the different phases of occupation of the island.

## ACKNOWLEDGMENT

Financial support was provided by Sapienza University of Rome (Ateneo funding, 2021) and PRIN 2017 Project People of the Middle Sea. Innovation and integration in ancient Mediterranean (1600–500 BC) [B.2. Innovative metallurgy] was funded by the Italian Ministry of Education, University and Research. PhD grants of the Department of Earth Sciences, Sapienza University of Rome, are gratefully acknowledged.

## CONFLICT OF INTEREST

The authors declare that they have no known competing financial interests or personal relationships that could have appeared to influence the work reported in this paper.

## ORCID

Caterina De Vito  <https://orcid.org/0000-0002-2083-776X>

## REFERENCES

- [1] N. M. Piatak, M. B. Parsons, R. R. Seal, *Appl. Geochem.* **2015**, 236.
- [2] B. Gorai, R. K. Jana, *Resour. Conserv. Recycl.* **2003**, 39, 299.
- [3] A. Hauptmann, *Archaeometallurgy in Global Perspective*, Springer, New York **2014**, p. 91.
- [4] X. Wang, D. Geysen, S. V. P. Tinoco, N. D'Hoker, T. Van Gerven, B. Blanpain, *Trans. Institutions min. Metall. Sect. C Miner. Process. Extr. Metall.* **2015**, 124, 83.
- [5] P. Costagliola, M. Benvenuti, L. Chiarantini, S. Bianchi, F. Di Benedetto, M. Paolieri, L. Rossato, *Appl. Geochem.* **2008**, 23, 1241.
- [6] T. H. Rehren, E. Pernicka, *Archaeometry* **2008**, 50, 232.
- [7] V. Workman, A. M. Maeir, A. Elyahu-behar, *J. Archaeol. Sci. Rep.* **2021**, 36, 102803.
- [8] M. Emami, T. Kowald, R. Trettin, *Archaeol. Anthropol. Sci.* **2017**, 9, 1515.
- [9] D. Bourgarit, *Eur. Mineral. Union Notes Mineral.* **2019**, 20, 203.
- [10] M. Radivojević, B. W. Roberts, E. Pernicka, Z. Stos-Gale, M. Martín-Torres, T. Rehren, P. Bray, D. Brandherm, J. Ling, J. Mei, H. Vandkilde, K. Kristiansen, S. J. Shennan, C. Broodbank, *The provenance, use, and circulation of metals in the European bronze age: The state of debate*, Vol. 27, Springer, US **2019** 131.
- [11] V. Serneels, S. Perret, *Proc. Int. Conf.* **2003**, 1, 469.
- [12] A. Elyahu-Behar, N. Yahalom-Mack, Y. Gadot, I. Finkelstein, *J. Archaeol. Sci.* **2013**, 40, 4319.
- [13] H. G. Bachmann, Routledge, **1982**.
- [14] C. P. Thornton, T. Rehren, V. C. Pigott, *J. Archaeol. Sci.* **2009**, 36, 308.
- [15] M. Bernabale, L. Nigro, C. Vaccaro, M. Nicoli, D. Montanari, P. Bigini, C. De Vito, *J. Raman Spectrosc.* **2022**, 53(2), 272.
- [16] T. de Caro, D. Caschera, G. M. Ingo, P. Calandra, *J. Raman Spectrosc.* **2016**, 47, 852.
- [17] T. de Caro, *J. Cult. Herit.* **2017**, 28, 65.
- [18] T. de Caro, C. Riccucci, E. I. Parisi, F. Faraldi, D. Caschera, *Appl. Phys. A: Mater. Sci. Process.* **2013**, 113, 945.
- [19] B. Kaufman, R. Docter, D. A. Scott, F. Chelbi, B. M. Telmini, *Archaeol. Anthropol. Sci.* **2019**, 11, 4075.
- [20] H. G. Niemeyer, *Mediterr. Archaeol.* **2001**, 14, 83.
- [21] M. Renzi, I. Montero-Ruiz, M. Bode, *J. Archaeol. Sci.* **2009**, 36, 2584.
- [22] L. Nigro, D. Montanari, F. Mura, M. Bernabale, C. De Vito, *Vicin. Oriente.* **2020**, 24, 57.
- [23] F. Spagnoli, in *Religious Convergence in the Ancient Mediterranean*, (Eds: S. Blakely, B. J. Collins), ISD LLC, Atlanta **2019**, p. 329.
- [24] M. Bernabale, L. Nigro, D. Montanari, C. De Vito, *J. Cult. Herit.* **2021**, 52, 146.
- [25] L. Nigro, *Entre Utica y Gadir: navegación y colonización fenicia en el Mediterráneo Occidental a comienzos del I Milenio*, Comares, Granada **2020**, p. 97.
- [26] C. Giardino, *Early Soc. Sicily. New Dev. Archaeol. Res.* **1996**, 5, 129.
- [27] A. Corretti, M. Benvenuti, *Mediterr. Archaeol.* **2001**, 14, 127.
- [28] K. Kądziołka, A. Pietranik, J. Kierczak, A. Potysz, T. Stolarczyk, *J. Archaeol. Sci.* **2020**, 118, 105142.
- [29] M. Di Fazio, A. C. Felici, F. Catalli, C. De Vito, *Sci. Rep.* **2019**, 9, 1.
- [30] F. Di Turo, F. Coletti, C. De Vito, *Microchem. J.* **2020**, 157, 104882.
- [31] A. Doménech-Carbó, B. Ramírez-Barat, C. Petiti, S. Goidanich, M. T. Doménech-Carbó, E. Cano, *J. Electroanal. Chem.* **2020**, 877, 114494.
- [32] L. Nigro, *Sci. dell'Antichità* **2016**, 22, 339.
- [33] L. Nigro, *Mozia-XII. Zona D. La" Casa del sacello domestico", il" Basamento meridionale" e il Sondaggio stratigrafico I. Rapporto preliminare delle campagne di scavi XXIII e XXIV (2003-2004)*, Lorenzo Nigro, **2011**.
- [34] F. Spagnoli, *Water Urban. A Hist. Water Ser. III* **2014**, 1, 89.
- [35] L. Nigro, F. Spagnoli, *Alle sorgenti del Kothon: il rito a Mozia nell'area sacra di Baal'Addir-Poseidon: lo scavo dei pozzi sacri nel settore C Sud-ovest (2006-2011)*, Lorenzo Nigro, **2012**, 2.
- [36] L. Nigro, *La vie, la mort et la religion dans l'univers phénicien et punique in Actes du VIIème Congrès International des Études Phéniciennes et Puniqes*, Institut National du Patrimoine **2019**, p. 1641.

- [37] F. Rademakers, PhD Thesis, **2015**.
- [38] S. Liu, T. Rehren, J. Chen, C. Xu, P. Venunan, D. Larreina-garcia, M. Martin, **2015**, 55, 151.
- [39] H. Hugh Mckerrell, R. F. Tylecote, *Proc. Prehist. Soc.* **1972**, 38, 209.
- [40] R. F. Tylecote, H. A. Ghaznavia, P. J. Boydell, *J. Archaeol. Sci.* **1977**, 4, 305.
- [41] M. Hasegawa, in *Treatise on Process Metallurgy*, Elsevier **2014**, p. 507.
- [42] T. Rehren, L. Boscher, E. Pernicka, *J. Archaeol. Sci.* **2012**, 39, 1717.
- [43] V. Ettler, R. Červinka, Z. Johan, *Archaeometry* **2009**, 51, 987.
- [44] M. Vítková, V. Ettler, Z. Johan, B. Křibek, O. Šebek, M. Mihaljevič, *Mineral. Mag.* **2010**, 74, 581.
- [45] C. Mapelli, W. Nicodemi, R. F. Riva, *ISIJ Int.* **2007**, 47, 1050.
- [46] C. H. Donaldson, *Mineral. Petrol.* **1976**, 57, 187.
- [47] H. Portillo, M. C. Zuluaga, L. A. Ortega, A. Alonso-Olazabal, X. Murelaga, A. Martinez-Salcedo, *Microchem. J.* **2018**, 138, 246.
- [48] R. L. Frost, *Spectrochim. Acta - Part a Mol. Biomol. Spectrosc.* **2003**, 59, 1195.
- [49] S. Kyoung, P. In, C. Kwon, S. Jeong, L. Il, K. Huh, N. Chul, *J. Conserv. Sci.* **2019**, 35, 145.
- [50] G. Bertolotti, D. Bersani, P. P. Lottici, M. Alesiani, T. Malcherek, *Anal. Bioanal. Chem.* **2012**, 402, 1451.
- [51] M. Bouchard, D. C. Smith, *Spectrochim. Acta - Part a Mol. Biomol. Spectrosc.* **2003**, 59, 2247.
- [52] T. De Caro, E. Angelini, L. E. Sebar, *Acta Imeko* **2021**, 10, 234.
- [53] L. Toffolo, *J. Archaeol. Sci. Rep.* **2018**, 19, 248.
- [54] P. T. Craddock, N. D. Meeks, *Archaeometry* **1987**, 29, 187.
- [55] Y. Bassiakos, M. Catapotis, *Chrysokamino Metall. Work. Territ. (Hesperia Suppl. 36)* **2006**, 36, 329.
- [56] D. Ashkenazi, O. Golan, O. Tal, *Archaeometry* **2013**, 55, 235.
- [57] O. Oudbashi, M. Mishmastnehi, *J. Archaeol. Sci. Rep.* **2020**, 30, 102216.
- [58] E. F. Osborn, A. Muan, *Phase Equilibrium Diagrams of Oxide Systems*, American Ceramic Society with the Edward Orton Jr. Ceramic Foundation, Columbus **1960**.
- [59] S. Paynter, P. Crew, E. Blakelock, G. Hatton, *Hist. Metall.* **2015**, 49, 126.
- [60] M. F. Charlton, E. Blakelock, M. Martín-Torres, T. Young, *J. Archaeol. Sci.* **2012**, 39, 2280.
- [61] A. Manasse, M. Mellini, C. Viti, *Eur. J. Mineral.* **2001**, 13, 949.
- [62] S. F. Muralha, R. J. H. Clark, *J. Raman Spectrosc.* **2011**, 42, 2077.
- [63] K. Westner, PhD Thesis, **2016**, 429.
- [64] O. Oudbashi, D. Agha-Aligol, M. Mishmastnehi, V. Barnoos, *Archaeol. Anthropol. Sci.* **2019**, 11, 2059.
- [65] Q. Wang, S. Strekopytov, B. W. Roberts, *J. Archaeol. Sci.* **2018**, 97, 102.
- [66] M. Murillo-Barroso, M. Martín-Torres, M. D. C. Massieu, D. M. Socas, F. M. González, *Archaeol. Anthropol. Sci.* **2017**, 9, 1539.
- [67] B. Höppner, M. Bartelheim, M. Huijsmans, R. Krauss, K. P. Martinek, E. Pernicka, R. Schwab, *Archaeometry* **2005**, 47, 293.
- [68] S. R. B. Cooke, S. Aschenbrenner, *J. F. Archaeol.* **1975**, 2, 251.
- [69] R. Maddin, J. D. Muhly, *JOM* **1974**, 26, 24.
- [70] C. Saccà, D. Saccà, P. Nucera, A. De Fazio, G. Pisacane, *AAPP Atti Della Accad. Peloritana Dei Pericolanti, cl. di Sci. Fis. Mat. E Nat.* **2006**, 84, 1.
- [71] M. Moroni, S. Naitza, G. Ruggieri, A. Aquino, P. Costagliola, G. De Giudici, S. Caruso, E. Ferrari, M. L. Fiorentini, P. Lattanzi, *Ore Geol. Rev.* **2019**, 115, 103194.
- [72] P. Valério, R. J. C. Silva, A. M. M. Soares, M. F. Araújo, A. P. Gonçalves, R. M. Soares, *Nucl. Instruments Methods Phys. Res. Sect. B Beam Interact. Mater. Atoms* **2015**, 358, 117.
- [73] N. L. Erb-Satullo, D. Jachvliani, K. Kakhiani, R. Newman, *J. Archaeol. Sci.* **2020**, 123, 105220.

## SUPPORTING INFORMATION

Additional supporting information can be found online in the Supporting Information section at the end of this article.

**How to cite this article:** M. Bernabale, D. Montanari, L. Nigro, F. Spagnoli, C. Vaccaro, N. Eftekhari, M. Nicoli, C. De Vito, *J Raman Spectrosc* **2023**, 54(1), 54. <https://doi.org/10.1002/jrs.6453>